

A Fractional-N Digitally Intensive PLL Achieving 428-fs Jitter and <-54 -dBc Spurs Under 50-mV_{pp} Supply Ripple

Chen, Yue; Gong, Jiang; Staszewski, Robert Bogdan; Babaie, Masoud

DOI

[10.1109/JSSC.2021.3123386](https://doi.org/10.1109/JSSC.2021.3123386)

Publication date

2022

Document Version

Final published version

Published in

IEEE Journal of Solid-State Circuits

Citation (APA)

Chen, Y., Gong, J., Staszewski, R. B., & Babaie, M. (2022). A Fractional-N Digitally Intensive PLL Achieving 428-fs Jitter and <-54 -dBc Spurs Under 50-mV_{pp} Supply Ripple. *IEEE Journal of Solid-State Circuits*, 57(6), 1749-1764. <https://doi.org/10.1109/JSSC.2021.3123386>

Important note

To cite this publication, please use the final published version (if applicable). Please check the document version above.

Copyright

Other than for strictly personal use, it is not permitted to download, forward or distribute the text or part of it, without the consent of the author(s) and/or copyright holder(s), unless the work is under an open content license such as Creative Commons.

Takedown policy

Please contact us and provide details if you believe this document breaches copyrights. We will remove access to the work immediately and investigate your claim.

A Fractional- N Digitally Intensive PLL Achieving 428-fs Jitter and <-54 -dBc Spurs Under 50-mV_{pp} Supply Ripple

Yue Chen¹, Student Member, IEEE, Jiang Gong², Student Member, IEEE,
Robert Bogdan Staszewski³, Fellow, IEEE, and Masoud Babaie⁴, Member, IEEE

Abstract—In this article, we present a 4.5–5.1-GHz fractional- N digitally intensive phase-locked loop (DPLL) capable of maintaining its performance in face of a large supply ripple, thus enabling a direct connection to a switched-mode dc–dc converter. Supply pushing of its inductor–capacitor (LC) oscillator is suppressed by properly replicating the supply ripple onto the gate of its tail current transistor, while the optimum replication gain is determined by a new on-chip calibration loop tolerant of supply variations. A proposed configuration of cascading a supply-insensitive slope generator with an output of a current digital-to-analog converter (DAC) linearly converts the phase error timing into a corresponding voltage, which is then quantized by a successive approximation register (SAR) analog-to-digital converter (ADC) to generate a digital phase error. We also introduce a low-power ripple pattern estimation and cancellation algorithm to remove the phase error component due to the supply-induced delay variations of loop components. Implemented in 40-nm CMOS, the DPLL prototype achieves the performance of 428-fs rms jitter, <-55 -dBc fractional spur, and <-54 -dBc maximum spur while consuming 3.25 mW and being subjugated to a sinusoidal or sawtooth supply ripple of 50 mV_{pp} at 50-MHz reference divided by 3, 6, or 12.

Index Terms—Current digital-to-analog converter (DAC), dc–dc converter, digitally intensive phase-locked loop (DPLL), inductor–capacitor (LC) oscillator, multimodulus divider (MMDIV), resample, ripple pattern estimation and cancellation, ripple replication and cancellation, slope generator (SG), successive approximation register (SAR) analog-to-digital converter (ADC), supply pushing, supply ripple.

Manuscript received May 27, 2021; revised September 12, 2021; accepted October 21, 2021. Date of publication November 12, 2021; date of current version May 26, 2022. This article was approved by Associate Editor Daniel Friedman. This work was supported in part by the Netherlands Organization for Scientific Research under Project 13598 and Project 17303; and in part by the National Science Center, Poland, under Contract UMO-2017/27/B/ST7/01217. (Corresponding author: Yue Chen.)

Yue Chen and Masoud Babaie are with the Department of Microelectronics, Delft University of Technology, 2628 CD Delft, The Netherlands (e-mail: y.chen-1@tudelft.nl).

Jiang Gong is with the Department of Quantum and Computer Engineering, Delft University of Technology, 2628 CJ Delft, The Netherlands.

Robert Bogdan Staszewski is with the School of Electrical and Electronic Engineering, University College Dublin, Dublin 4, Ireland, also with the Department of Microelectronics, Delft University of Technology, 2628 CD Delft, The Netherlands, and also with the Department of Measurement and Instrumentation, AGH University of Science and Technology, 30-059 Kraków, Poland.

Color versions of one or more figures in this article are available at <https://doi.org/10.1109/JSSC.2021.3123386>.

Digital Object Identifier 10.1109/JSSC.2021.3123386

I. INTRODUCTION

INTEGRATED circuits and systems are generally powered by switch-mode dc–dc converters, which transforms the voltage level of an energy source into the system’s nominal supply voltage with sufficiently high efficiency [1]. However, if the dc–dc converter directly supplies sensitive analog or RF circuits, such as oscillators and phase-locked loops (PLLs), its output ripples could severely degrade their performance. Consequently, a low dropout (LDO) linear regulator is typically inserted after the switching converter to suppress the ripples. When the dominant pole of the LDO is located at its output, the load capacitor could be as large as several microfarads to guarantee the loop stability, thus necessitating the use of external capacitors. Hence, following the trend of full-system integration, the “capacitor-less” LDO topology with the dominant pole located at the output of the error amplifier (EA) is preferred. However, to isolate the sensitive oscillator from the clocked phase detection circuitry, PLLs usually require two separate LDOs [2], thereby worsening the system complexity and cost. The power efficiency of the LDO is related to both its dropout voltage (V_{DO}) and the quiescent current flowing through the EA (I_{EA}) and through the feedback resistor (I_F). The ~ 100 -mV V_{DO} , established by the required power supply rejection (PSR) performance, consumes extra voltage headroom and degrades system efficiency by a factor of $\sim 0.9\times$ at a 1-V supply [3]. The levels of I_{EA} and I_F are mainly determined by the figure of merit (FoM) of the oscillator (FoM_{osc}) and loop (FoM_{loop}) components [4] for the corresponding LDOs, respectively. The analysis in [3] shows that the efficiency of the LDO powering the oscillator could further drop by a factor of ~ 0.7 – $0.8\times$ due to the quiescent current. Consequently, it deems beneficial if the PLL could be powered directly from the dc–dc converter, thus entirely avoiding the LDOs.

The implementation of such a PLL faces several challenges. First, since the switched-capacitor-based dc–dc converters are generally clocked at several or tens of MHz, the induced variation on oscillator frequency could hardly be suppressed by PLLs with a typical bandwidth of <1 MHz.¹ Hence, several

¹Note that the transfer function from the oscillator output to the PLL output is high pass.

techniques have been proposed in the literature to reduce the supply pushing of the oscillator [5]–[15]. However, most of these techniques are only effective for tiny (e.g., 1 mV) [5] or low frequency (<1 MHz) [6], [7], [10], [13] supply ripples or would require high power and area overhead [11], [12]. In [9], the PLL loop needs to be periodically opened for calibration. In [14], a test signal that is slow enough compared to the PLL bandwidth is applied on the supply of a ring oscillator, but this could lead to a long calibration time of more than hundreds of microseconds. Moreover, unlike in the ring oscillator [9], [14], it is difficult to modulate the supply of an inductor–capacitor (LC) oscillator. In [16], we have proposed a feedforward ripple replication and cancellation technique for an LC oscillator. However, similar to [12], its calibration loop still requires a “clean” supply.

Besides the oscillator, the delay and transfer function of the PLL’s other building blocks are also modulated by the supply ripple, thus contributing to the phase error perturbation at the output of a phase detector (PD). This increases the PLL output spurs, mainly at the ripple frequency, f_{rip} , and its harmonics. Moreover, in a fractional- N operation, the fractional frequency (f_{frac}) inter-modulates with f_{rip} due to the PD nonideality, generating output spurs at the intermodulation frequencies ($f_{\text{rip}} \pm f_{\text{frac}}$). Nevertheless, in the scarcely available literature on PLLs with reduced supply sensitivity, mainly the integer- N operation is considered [2], [17], while the intermodulation problem between f_{rip} and f_{frac} of fractional- N operation is seldom discussed.²

In contrast to its analog counterpart, a highly digitally intensive PLL (DPLL) features the natural ability to exploit various digital calibration techniques to tackle the aforementioned issues with relative ease. Consequently, a DPLL is favored when architecting for the direct powering by the switched-mode dc–dc converter. In this article, we propose a digital-to-analog converter (DAC)-assisted fractional- N DPLL architecture to enable direct operation under a large 50-mV_{pp} supply ripple. The reduced supply sensitivity of the proposed voltage-domain PD suppresses the intermodulated terms, while the effect of the supply-induced delay variation is canceled through digital calibration. The supply pushing of the LC oscillator is also reduced through the feedforward cancellation technique with an improved calibration loop.

This article is organized as follows. Section II provides a detailed analysis of the issues encountered by directly powering the PLL from the converter. The proposed loop structure is derived in Section III. The detailed circuit implementations of different DPLL blocks are discussed in Section IV, while measurement results are provided in Section V.

II. DESIGN CHALLENGES WHEN SUPPLYING PLL WITH LARGE RIPPLE

This section investigates the effects of supply ripple on the PLL’s spectral purity. Note that although the DPLL structure is chosen as an example in a portion of the following analysis, the result is also valid for analog PLLs.

²Note that the intermodulation effect analyzed in [18] and [19] is between the reference frequency and the oscillation frequency, generating fractional spurs, which is not similar to the effect mentioned here.

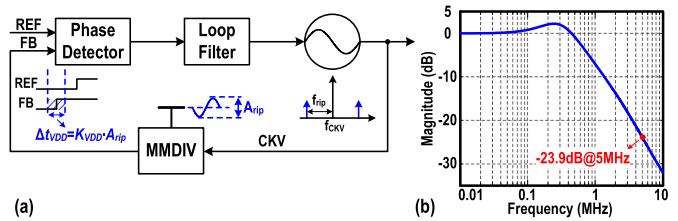


Fig. 1. (a) Spurs produced by the supply ripple modulating the divider output delay. (b) Magnitude response of a type-II PLL with a typical 300-kHz bandwidth and a damping factor of 0.707.

A. Spurs Due to Oscillator Supply Pushing

It is well known that the level of spurious tones around the carrier, induced by a sinusoidal supply ripple with a peak-to-peak amplitude of A_{rip} and a frequency of f_{rip} , can be estimated by

$$S_{\text{osc}} = 20 \cdot \log_{10} \left(\frac{K_{\text{push}} \cdot A_{\text{rip}}}{4 f_{\text{rip}}} \right) \quad (1)$$

where K_{push} is the supply pushing of the oscillator. From (1), to guarantee < -50 dBc spur level under a 50-mV_{pp} ripple, K_{push} should be less than 1.26 MHz/V, which is much lower than that of state-of-the-art RF oscillators [20]. To tackle this issue, the feedforward cancellation technique with an improved calibration loop is introduced in Section IV-D to improve the oscillator’s supply sensitivity.

B. Spurs Due to Delay Perturbations of PLL’s Components

Supply ripples also degrade the PLL’s spectral purity by modulating the delay of the edge-critical loop components. Fig. 1(a) shows an example in which the propagation delay of the multimodulus divider (MMDIV) is affected by its supply voltage. This delay variation is then sensed by the PD and transferred to the PLL’s output, leading to spurs at f_{rip} from the carrier. Assuming that the delay deviation is proportional to its supply perturbation A_{rip} , the spur level can be calculated as

$$S_{\text{dly}} = 20 \cdot \log_{10} \left(\frac{\pi \cdot K_{\text{VDD}} \cdot A_{\text{rip}}}{2 T_{\text{CKV}}} \right) + \text{TF}_{\text{loop}} \quad (2)$$

where K_{VDD} is the supply sensitivity of the MMDIV delay, T_{CKV} is the oscillator period, and TF_{loop} expresses the amount of dB attenuation provided by the loop. A detailed derivation of (2) is provided in Appendix A. The magnitude response of a type-II DPLL with a typical 300-kHz bandwidth is shown in Fig. 1(b). Note that a wider bandwidth would result in a lower attenuation by the loop (TF_{loop}), worsening the spur performance due to the delay variation, while a narrower bandwidth would provide less filtering of the oscillator phase noise (PN), consequently affecting the in-band PN and jitter performance of the loop [4]. For a 5-MHz f_{rip} , the suppression offered by the loop is only -23.9 dB. Hence, with a simulated $K_{\text{VDD}} \approx 400$ ps/mV, a 50-mV_{pp} ripple causes an approximately -40 -dBc spur at a 5-GHz carrier. Therefore, extra techniques will be introduced in Section IV-C3 in order to suppress the effect of this delay variation and to reduce the corresponding spurs.

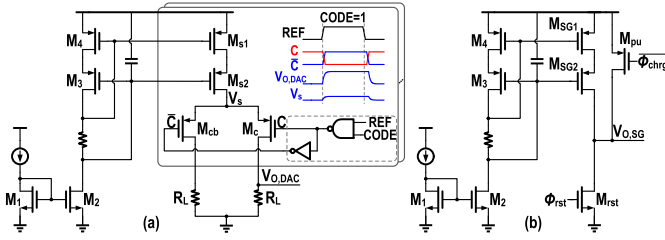


Fig. 6. Schematic of (a) current DAC and (b) slope generator.

DAC voltage resolution. When it is accurately estimated, the sampled V_{DAC} can be calculated by

$$\begin{aligned} V_{DAC} &= V_{DAC,os} + n_{DAC} \times V_{res} \\ &= V_{DAC,os} + (E_{q,max} - E_q) \times T_{CKV} \times (I_{SG}/C_{SG}) \quad (9) \end{aligned}$$

where $V_{DAC,os}$ is an offset voltage independent of n_{DAC} . In the next step, ϕ_{comb} , V_{SG} , and V_{DAC} are combined by connecting the top plate of C_{DAC} to the bottom plate of C_{SG} through S_4 . By summing (7) and (9), the generated ADC input voltage becomes

$$\begin{aligned} V_{IN} &= t_n \times (I_{SG}/C_{SG}) \\ &+ [V_{DAC,os} + (I_{SG}/C_{SG}) \times (t_{os} + E_{q,max} \times T_{CKV})]. \quad (10) \end{aligned}$$

The second term in (10) is time-invariant related to t_{os} . Due to the feedback operation of the loop, t_{os} will be adjusted automatically such that the corresponding term settles to the ADC's reference level, V_{ref} . Therefore, the ADC only needs to convert the input variations related to t_n . Note that the system is designed so that $V_{DAC,os}$ and the C_{SG} charge due to t_{os} equally provide the required input dc offset. Hence, the maximum voltage on the C_{SG} and C_{DAC} capacitors is limited to $\sim V_{ref}/2$, providing enough voltage headroom for the PMOS current sources to operate linearly. In contrast, the DAC and slope generator in [40] sequentially charge the same capacitor to $\sim V_{ref}$. This reduces the voltage headroom of the slope generator's current source, substantially degrading its linearity in a deep sub-micrometer technology with reduced supply.

2) *Circuit Design*: Fig. 6(a) shows the DAC schematic, consisting of 290 unary cascode current sources to satisfy the range and linearity requirements. As the DAC is biased through the current mirror, the DAC output variation due to the supply ripple can be estimated by

$$V_{O,DAC} \approx \frac{R_L}{R_L + r_{o,s1} + r_{o,s2} + g_{m,s2}r_{o,s1}r_{o,s2}} \cdot A_{rip} \quad (11)$$

where $g_{m,s1(2)}$ and $r_{o,s1(2)}$ are the small-signal transconductance and output resistance of $M_{s1(2)}$, respectively. Equation (11) shows that the high output impedance of the cascode structure is also beneficial in suppressing the supply-induced variation at the DAC output, and consequently, $M_{s1,2}$ are implemented as long-channel devices. During the output current transition from one branch to the other, the voltage across the current source, as observed at V_s , is affected. This dynamic disturbance couples to the bias voltage of the current mirror through the parasitic capacitance of $M_{s1,2}$, degrading the DAC settling speed and linearity. To alleviate this issue, dynamic element

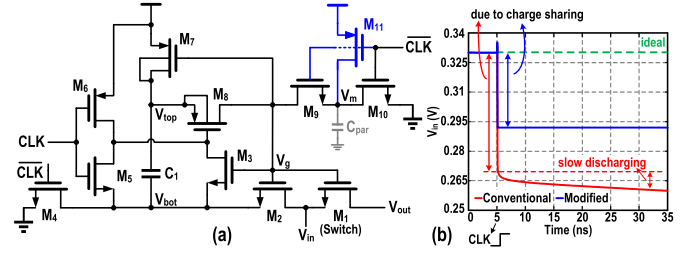


Fig. 7. (a) Schematic of the bootstrap switch. (b) Simulated performance of S_4 during the tracking phase.

matching is employed to relax the matching requirements [43] and to reduce the M_{s1} size and parasitic capacitance. Moreover, to remove the dependence of the output transition on the previous DAC samples, a return-to-zero encoding is adopted here by resetting the DAC output before each conversion. The implementation of the slope generator is shown in Fig. 6(b). Similar to the current DAC, a cascode current source is employed for better linearity and reduced supply sensitivity. After the output voltage, $V_{O,SG}$, has been sampled on C_{SG} , the pull-up transistor, M_{pu} , will pull the output node to the supply in order to suppress any leakage current through switch S_1 during the following steps (see Fig. 5).

A bootstrap technique, as shown in Fig. 7, is employed to implement the sampler ($S_{1,3}$) and voltage combiner (S_4) switches of Fig. 5 for the purpose of minimizing their ON-resistance. In the conventional bootstrap switch [44], [45], due to the reliability considerations of M_{10} , NMOS M_9 with its gate directly connected to supply is added to charge V_m to around $V_{DD} - V_{th}$ during the tracking phase. However, since M_9 is on the verge of turning on, its equivalent resistance is not large enough to suppress the leakage. Unlike in ADC designs, where the input is normally considered a "voltage source," the input of S_4 is stored as charge on C_{DAC} [see Fig. 5(c) and (d)]. Therefore, the leakage through M_9 causes the input level to decrease slowly during the tracking phase, ultimately leading to the nonlinearity during the ADC conversion. To overcome this, the M_9 gate is also connected to \overline{CLK} , and M_{11} is added to pull-up V_m to fully turn off M_9 during the tracking phase, providing a large enough OFF-resistance. With the new design, simulations prove that V_{in} remains constant, and the initial drop due to the charge sharing with parasitic capacitance is compensated by the K_{DAC} estimation. Since V_{in} is less than 360 mV in this design, $M_{9,10}$ should not suffer from any reliability issues.

The comparator used in the SAR ADC is shown in Fig. 8(a). During the comparison (i.e., $CLK = 1$), the voltage perturbation at the internal nodes is coupled to the input, disturbing the input voltage and comparator's decision. To alleviate this kickback effect, dummy capacitors [see the red dotted region in Fig. 8(a)] and a sampling switch (M_{ref}) are placed at the other input of the comparator to sample the reference voltage, $V_{ref,samp}$, in every reference cycle. Both V_{IN} and $V_{ref,samp}$ are affected similarly by the kickback, and consequently, the comparator can decide correctly, as shown in Fig. 8(b). Moreover, the supply ripple can also couple to the comparator's inputs through the drain-source/gate-drain parasitic capacitance of M_{SG}/M_{ref} , potentially affecting the comparator's decision.

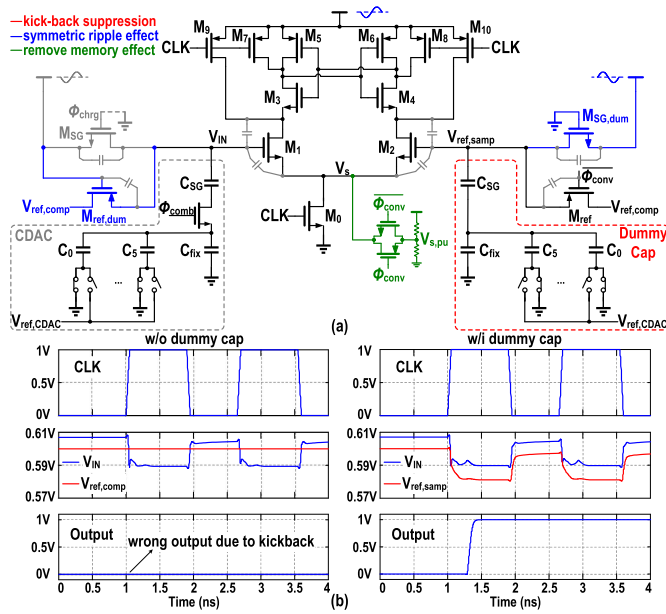


Fig. 8. (a) Schematic of the comparator in SAR ADC. (b) Simulation results of its kickback effect.

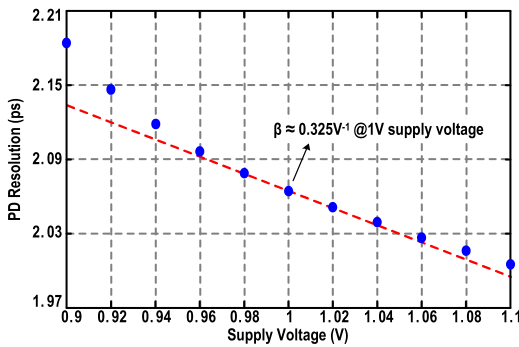


Fig. 9. Simulated supply sensitivity of the PD.

Hence, two dummy switches, $M_{SG,dum}$ and $M_{ref,dum}$, are also inserted [see the components in blue in Fig. 8(a)] such that the supply ripple appears as a common-mode (CM) voltage at the comparator's inputs, thus securing its seamless operation. Finally, the common-source node of $M_{1,2}$, V_s , is also pulled up to a fixed voltage during the charging and combining phases to remove the memory of the last conversion at the comparator's internal nodes [see the components in green in Fig. 8(a)].

Fig. 9 reports the simulated supply sensitivity of the implemented PD, reading $\beta \approx 0.325 V^{-1}$ around the 1-V supply, which is about 3.7–6.3 times lower than that of the conventional TDC/DTC. To further improve the spur performance, a second-order $\Delta\Sigma$ modulator is employed, as discussed in Section IV-B.

B. Divider and Resampler

The oscillator's frequency is divided down by a 6-bit MMDIV, implemented by cascading six stages of divide-by-2/3 cells [46]. A second-order $\Delta\Sigma$ modulator drives the MMDIV to randomize the pattern of division ratio, thereby

further suppressing the possible spurs at the intermodulation frequencies and ensuring proper convergence of the K_{DAC} calibration at near-integer channels. However, the maximum time duration in which the slope generator is active increases to $2T_{CKV}$ in this case. Hence, the dynamic range of V_{SG} is double in comparison with the first-order modulator case, thus compromising the linearity of the cascode current mirror in the slope generator. To reduce the maximum time error related to the high-order $\Delta\Sigma$ modulator, Tascia *et al.* [47] proposed to sequentially resample the divider output by the rising and falling edges of CKV with two flip-flops. Although a fixed timing relationship could be guaranteed in this way, the delay of the flip-flop could easily reach $0.5T_{CKV}$ at higher oscillation frequencies, leading to a metastability problem. In this design, the divider output is directly resampled in parallel by both the rising and falling edges of CKV (see Fig. 10). The following 2-to-1 MUX then selects between the two resampled outputs (DIV_r and DIV_f), realizing a quantization step of $0.5T_{CKV}$ and reducing the dynamic range of the slope generator to only one T_{CKV} ($\pm 0.5T_{CKV}$). The correct timing relationship is sensed by the sequence detect block and the result (R_{lead}) is provided to correctly control the divider. Besides, a tunable delay (t_d) is inserted before the rising-edge triggered resampling flip-flop and calibrated on-chip to avoid metastability. More details will be further elaborated in Section IV-C1.

The input to the $\Delta\Sigma$ modulator represents the fractional frequency ratio between the PLL output and the reference in the unit of the quantization step. Therefore, to correctly control the divider with its quantization step being halved through resampling, the input to the $\Delta\Sigma$ modulator, FCW_F , is doubled first, while the modulator output is divided by two to cancel this effect (see Fig. 4) since the divider itself is still an integer one. The integer part of the division result adds with the integer part of the frequency control word, FCW_I , to form the division ratio of MMDIV (N_{div}), while its fractional part is accumulated. By default, DIV_f leads DIV_r ($R_{lead} = 0$). Hence, the 1-bit sum of the accumulation (sel) controls the MUX to pass through DIV_f when the $0.5T_{CKV}$ time step is required, and when a carry-out signal is generated, N_{div} is further increased by 1. When DIV_r leads DIV_f ($R_{lead} = 1$), an extra 1 is added to N_{div} when DIV_r is selected to compensate for the reversed timing relation between $DIV_{f,r}$.

C. Digital Calibration

1) Calibration of t_d : Since the MMDIV is triggered by the falling edge of CKV, its output (DIV_{int}) may fall intolerably close to the CKV rising edge. Thus, a tunable delay (t_d) is inserted before the rising-edge triggered resampling flip-flop to avoid metastability. As shown in Fig. 10, the tunable delay block aligns its output (DIV_d) with the following falling edge of CKV so that the maximum setup and hold margin could be guaranteed when sampled by the CKV rising edge. To find the proper value of t_d , its control code is swept, and for each delay setting, the delayed output (DIV_d) is sampled by the falling edge of CKV to obtain the calibration input, CAL_{in} . The optimum control code is reached when CAL_{in} jumps from high to low. A similar principle is used in [48] to delay the

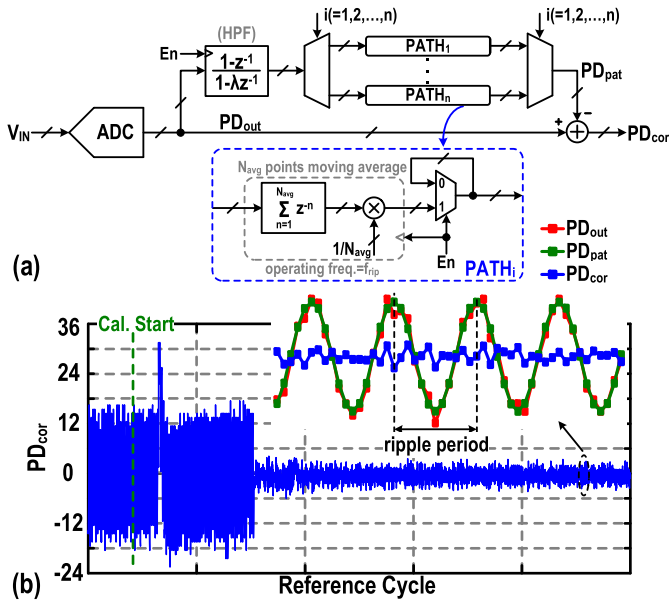


Fig. 11. (a) Block diagram of the ripple pattern estimation and cancellation. (b) Example of calibration waveform with $f_{rip} = f_{ref}/12$.

a large amount under the 50-mV_{pp} supply ripple considered here. Another LMS loop is also implemented to calibrate an average C_{mc} code for all reference cycles to simplify the calibration process. The detailed operation of the calibration process will be further discussed in Section IV-C4.

3) *Ripple Pattern Estimation and Cancellation*: As discussed in Section II-B, the output delay perturbations of MMDIV and resample flip-flops caused by the supply ripple are sensed by the PD, and thus, they appear as spurs at the DPLL output. The subsequent pattern estimation and cancellation block, shown in Fig. 11, is used to suppress this effect. Since the SAR ADC output, PD_{out} , shows a periodic digital pattern at f_{rip} due to supply-induced delay variations, the task of this digital block is to extract this pattern and subtract it from PD_{out} before modulating the oscillator. To do so, n ($= f_{ref}/f_{rip}$) branches ($PATHi$ in Fig. 11), each storing one different point of PD_{out} , are rotationally enabled. The N_{avg} -point moving-average filter in $PATHi$ is employed to suppress the random noise component in PD_{out} to guarantee accurate estimation of the f_{rip} pattern. A high-pass filter (HPF) is also inserted at the front. The HPF avoids the detected phase error at low-frequency offsets from entering the calibration loop and affecting the generated pattern PD_{pat} . Hence, the PN performance of the DPLL at low-frequency offsets would not be affected by this calibration. A similar algorithm is employed in [51] to suppress the fractional or external DPLL spurs, consuming ~ 2 mW for each calibration loop. In contrast, f_{ref}/f_{rip} in this design is a known integer determined during system planning, allowing us to avoid the need for the complex fractional delay filter and the extra calibration loop to optimize the filter coefficient, as in [51], resulting in a much lower power consumption. Meanwhile, after the accurate PD_{pat} is obtained, the extraction process is also turned off by disabling the enable signal (En). After that, only the output of each branch is preserved with all other calculations in the calibration loop disabled, which further reduces the

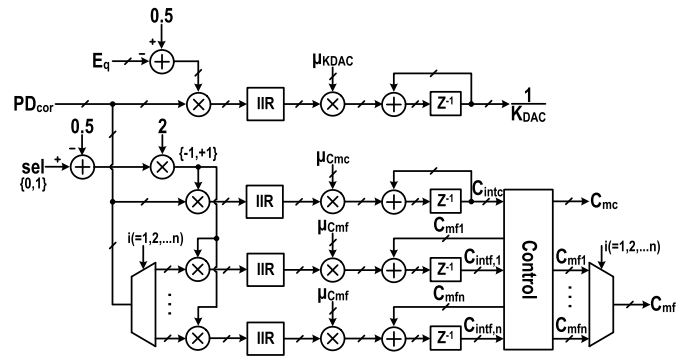


Fig. 12. Block diagram of the LMS calibration loops for the DAC gain and resampler's mismatch.

current consumption to ~ 80 μ A. Compared to the ~ 2 mW consumed by the loop components, the power efficiency is thus only degraded by $\sim 4\%$. The extraction process may also keep operating in the background to track environmental changes if needed, raising the power consumption to ~ 190 μ A. Otherwise, a simple digital threshold detector could be implemented to monitor PD_{cor} and only trigger the extraction process when PD_{cor} exceeds the predefined threshold value, lowering the extra power penalty.

Note that the algorithm cannot suppress the effect of supply noise. Hence, the PN induced by the supply noise is determined by the intrinsic supply sensitivity of the circuit, which is similar to conventional designs. Meanwhile, in the practical setting, the dc-dc converter typically shows a much lower output noise compared to LDOs [52]–[55], thus posing no significant degradation to the loop performance.

4) *Co-Operation of Calibration Loops*: The detailed block diagram of the LMS loops calibrating K_{DAC} and $C_{mc/f}$ is shown in Fig. 12. The error signal, PD_{cor} , is cross-correlated with $(0.5 - E_q)$ and also with the selection signal (sel) of the resampler's MUX. A simple first-order IIR filter follows to attenuate non-dc components after the correlation. Note that it is the inverse of K_{DAC} , $1/K_{DAC}$, that is actually being estimated so that the calculation of n_{DAC} is realized with a multiplier instead of a divider, thus saving power consumption and hardware. The estimation of the coarse C_{mc} and fine C_{mf} control codes is completed in two steps. First, the controller enables the LMS loop to calibrate for an average C_{mc} value over a predefined number of reference cycles. C_{mc} is then fixed and the corresponding LMS loop disabled while starting the calibration of the fine-tuning code C_{mf} . As discussed in Section IV-C2, C_{mf} is estimated cyclically through $n = f_{ref}/f_{rip}$ LMS loops (see Fig. 12), with the i th ($i = 1, \dots, n$) loop correlating the PD_{cor} and the sel signal of the $k \times n + i$ ($k = 1, 2, 3, \dots$) reference cycles. The individual results, $C_{intf,i}$, are monitored by the controller and directly passed onto $C_{mf,i}$ to form the C_{mf} sequence if they remain within the $[0, 48]$ range. When the limits are exceeded, the controller adds/subtracts 32 to/from $C_{intf,i}$ to generate the corresponding $C_{mf,i}$ while decreasing/increasing C_{mc} by two for the $k \times n + i$ reference cycles. Therefore, the fine-tuning range is extended with a minimal disturbance introduced during the LMS calibration process.

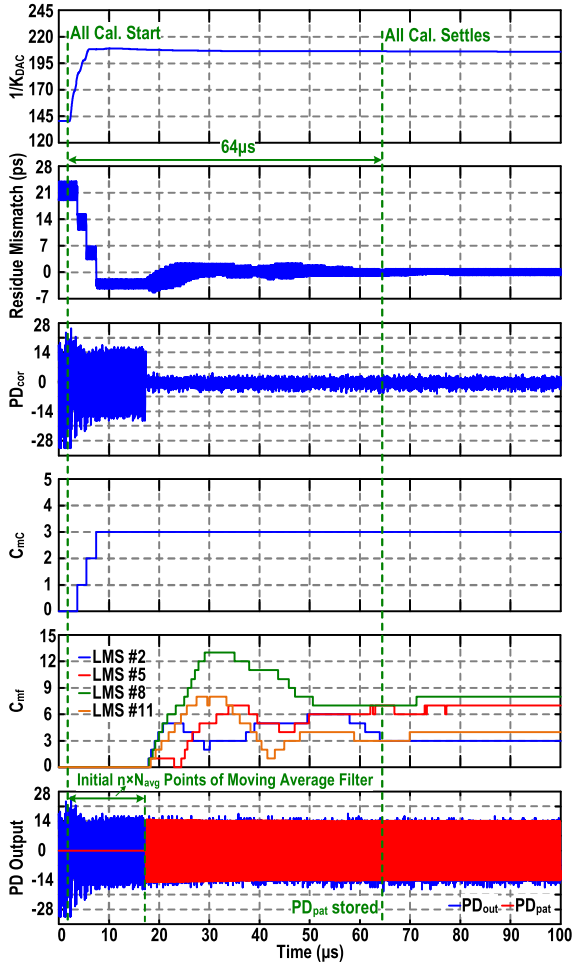


Fig. 13. Convergence trajectory of the calibration process with $f_{\text{rip}} = f_{\text{ref}}/12$.

Fig. 13 shows the simulated convergence trajectory of the calibration process with $f_{\text{rip}} = f_{\text{ref}}/12$. The induced mismatch is large to clearly demonstrate the settling behavior. In general, the implemented calibration loops could operate in parallel without a dedicated calibration sequence due to the difference in signal patterns they operate on: The signals that PD_{cor} is correlated with are related to f_{irac} , with $(0.5 - E_q)$ showing the high-pass shaped noise spectrum of the $\Delta\Sigma$ modulator and the sel signal being rich in discrete tones at f_{irac} and its harmonics, while the ripple pattern cancellation algorithm extracts the pattern at f_{rip} . To increase the settling speed, a larger integration step ($\mu_{\text{KDAC},0}$ and $\mu_{\text{Cmf},0}$) is employed initially and then gear-shifted to their final values of $\mu_{\text{KDAC},0}/32$ and $\mu_{\text{Cmf},0}/32$ in two steps under the control of a reference cycle counter in order not to affect the loop performance during the normal operation. As shown in Fig. 13, the settling time of the whole calibration process is $\sim 64 \mu\text{s}$ and is dominated by the C_{mf} calibration. For special cases of f_{irac} being close to f_{rip} or its harmonics, the frequency of the sel pattern becomes related to f_{rip} , and the interaction between the $C_{\text{mc}/f}$ calibration and the ripple pattern cancellation could impede the proper loop convergence. However, the problem could be avoided by disabling the $C_{\text{mc}/f}$ calibration in this scenario, while the ripple pattern estimation and cancellation block could cancel the effects of both the supply-induced delay perturbation and the

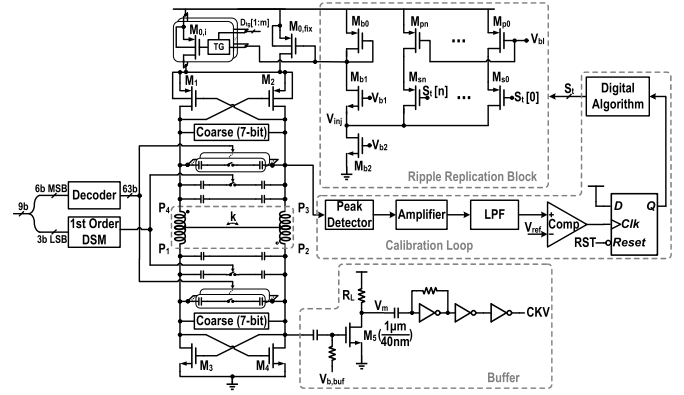


Fig. 14. Schematic of the LC oscillator with its calibration loop.

resampler's mismatch that is small enough as not to saturate the PD output.

D. LC Oscillator and Supply Pushing Calibration

The structure of the complementary LC oscillator is shown in Fig. 14. It consists of 7-bit 5.2-MHz/LSB binary and 63-bit 125-kHz/LSB unary switched capacitors for coarse and fine frequency tuning, respectively. An extra switched capacitor controlled by a first-order $\Delta\Sigma$ modulator is also added to further improve the frequency resolution to ~ 15 kHz. The first stage of the oscillator's buffer is implemented by an NMOS common-source amplifier with a load resistor. A tiny NMOS is intentionally used in this stage so that the variation of its input parasitic capacitance due to the supply ripples would not affect the oscillator's performance. Three stages of self-biased inverters then generate a rail-to-rail square wave that drives the MMDIV and the resampling flip-flops.

Similar to [16], a ripple replication block (RRB), controlled by the 6-bit $S_1[5:0]$ from the calibration loop, is designed to replicate the supply ripple to the gate of M_0 with a proper gain to stabilize the oscillator tail current and reduce its supply pushing. M_0 is implemented as a parallel combination of a fixed part, $M_{0,\text{fix}}$, with a bank of switchable unit transistors, $M_{0,i}$, to tune the tail current and, correspondingly, the oscillation swing. Compared to the conventional integration of an LDO with a current-biased oscillator in which the pass transistor of the LDO, M_{pass} , should be placed above the tail current source, the proposed technique performs both supply regulation and current tuning with only one transistor, thus saving the extra voltage headroom consumed by M_{pass} . Merging the tail transistor with M_{pass} might also reclaim the extra headroom, but the oscillator would then become voltage-biased whose current would be poorly controlled over PVT variations. Meanwhile, higher supply sensitivity of a voltage-biased oscillator could place higher demands on the PSR performance of the LDO, further degrading its power efficiency.

The calibration loop first detects and amplifies the variation of the oscillation amplitude. A digital algorithm then determines the optimum code to minimize that amplitude variation, thereby reducing spurious tones. The reduced supply pushing

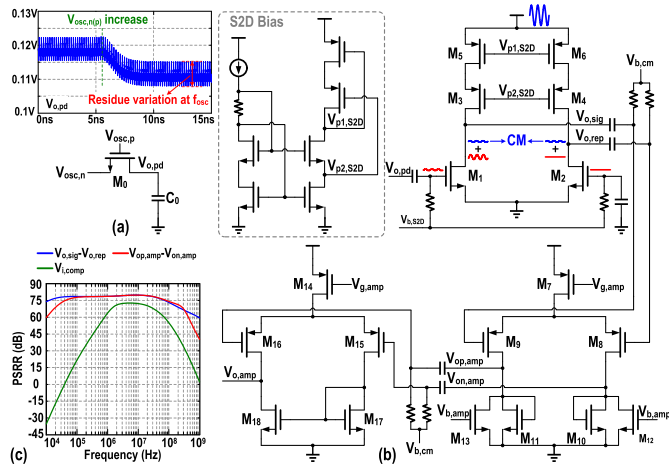


Fig. 15. Schematic of (a) peak detector and (b) amplifier chain in the oscillator calibration loop. (c) Simulated PSRR of the loop.

is also beneficial in significantly suppressing the conversion of thermal noise of supply to PN. Foreground calibration is selected due to the relatively relaxed spur requirement of the targeted applications (i.e., < -50 dBc) and the slow supply and temperature drifts of a low-power system whose effect could be compensated with intermittent recalibrations. In [16], the calibration loop needs to be powered with a clean supply to operate correctly. In this work, we tackle this issue by modifying the structure of the peak detector and amplification chain.

Fig. 15(a) shows the peak detector, consisting of an NMOS transistor, M_0 , and a load capacitor, C_0 . The gate and source terminals of M_0 are driven by the oscillator's differential output, $V_{osc,n(p)}$. Hence, M_0 acts as a switch and approximately turns ON for half of the oscillator cycle when $V_{osc,p} \geq V_{osc,n} + V_{th}$. During this phase, the low-pass filter formed by M_0 ON-resistance and C_0 filters out the high-frequency components and extracts the average value of this half-cycle, leading to a peak detection gain of $\sim 1/\pi$. Since the peak detector is not connected to the supply, its performance is not affected by the supply ripple.

Fig. 15(b) shows the amplifier chain located between the peak detector and comparator. Similar to the DAC current source, the first amplifier stage is implemented with a cascode PMOS current mirror for a higher PSR ratio (PSRR). We now inspect the outputs of the first-stage amplifier. The supply ripple and the peak detector voltage appear as CM and differential-mode (DM) signals, respectively. Therefore, when these signals are sent to the following differential amplifier stages, the desired signal is further amplified, while the supply-induced variations are suppressed by their CM rejection ratio (CMRR). As can be gathered from simulation results in Fig. 15(c), PSRR is higher than 60 dB at the comparator's input over the desired frequency range (i.e., 2–20 MHz), enough for the calibration loop to function correctly under the 50-mV_{pp} ripple.

V. MEASUREMENT RESULTS

The proposed fractional- N DPLL is implemented in TSMC 40-nm 1P8M CMOS without the customary ultra-thick metal

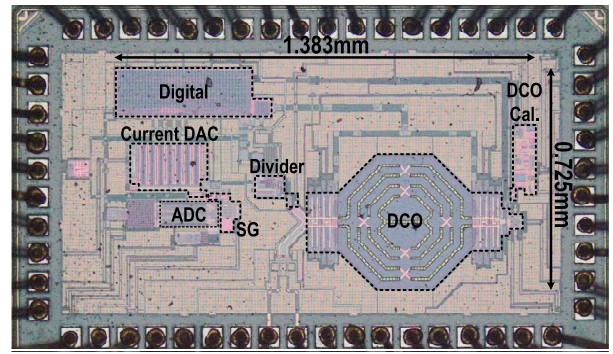


Fig. 16. Chip micrograph of the DPLL.

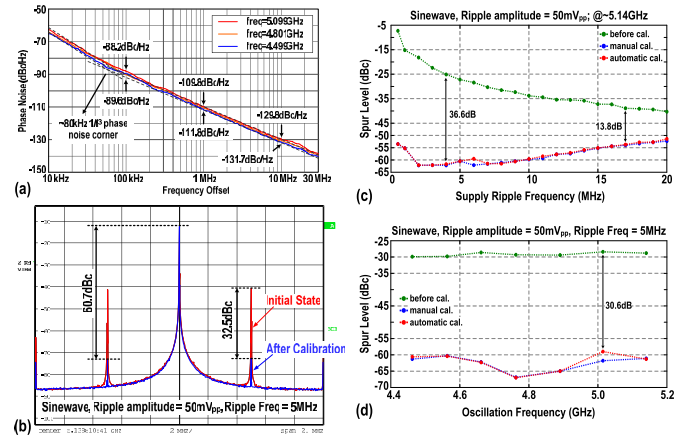


Fig. 17. Measurements of the free-running DCO: (a) PN across the TR; (b) spectrum before and after the automatic calibration in face of a 50-mV_{pp} 5-MHz sinusoidal ripple. Spur levels across (c) ripple frequency and (d) oscillation frequency for both the manual and automatic calibrations.

layers. Fig. 16 shows the chip micrograph. The DPLL has an active area of 0.39 mm², in which the oscillator, the current DAC, and the digital part occupy 0.157, 0.14, and 0.056 mm², respectively. Powered by a 1.0-V supply, the whole loop consumes 3.25 mW (1.02 mW for digitally controlled oscillator (DCO), 0.92 mW for PD, and 0.63 mW for the digital part).

The DPLL is first set to an open-loop mode to measure the performance of the free-running DCO. The measured tuning range (TR) is 4.47–5.14 GHz. Fig. 17(a) shows the measured PN performance across the TR. PN varies from -109.8 to -111.8 dBc/Hz at the 1-MHz offset, with a flicker noise corner around 80 kHz. The effectiveness of the modified calibration loop is verified in Fig. 17(b)–(d). In these measurements, a 50-mV_{pp} sinewave ripple is applied to the supply of the oscillator core and its calibration loop. Fig. 17(b) compares the oscillator spectrum before and after the calibration. Under the 50-mV_{pp} 5-MHz supply ripple, the measured spur level is reduced by 32.5 dB and reaches -60.7 dBc after the calibration. Fig. 17(c) shows the measured spur level over the frequency of the supply ripple. The oscillator exhibits lower than -51 -dBc spur level with the 0.5–20-MHz 50-mV_{pp} supply ripples, while the calibration loop is able to successfully find the optimum operating point in most cases. The improvement after the automatic calibration is between 13.8 and 36.6 dB for 4–17-MHz ripples. The rise of the spur level after the calibration at higher f_{rip} is due to the limited bandwidth of

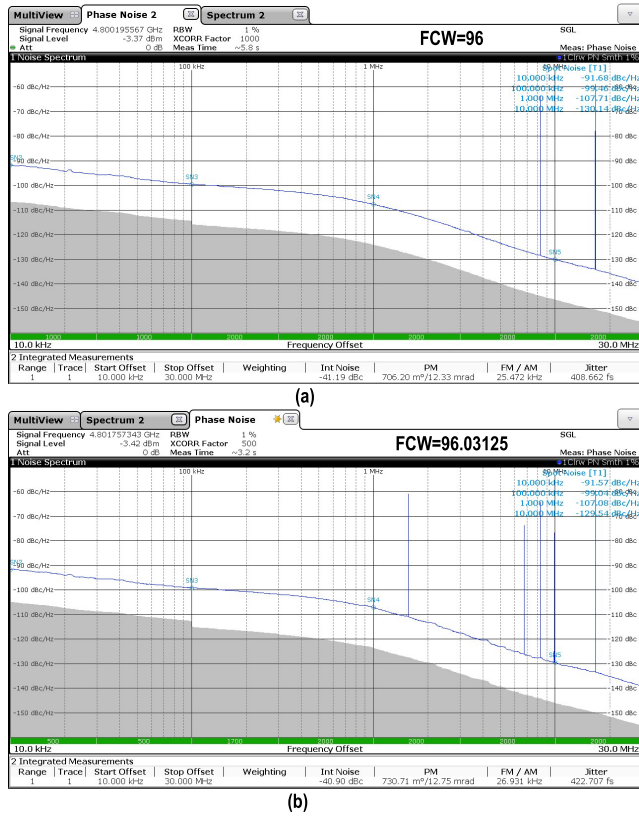


Fig. 18. Measured DPLL PN at (a) integer- N and (b) fractional- N channels around 4.8 GHz.

RRB since a phase shift between the supply ripple and its replica would result in a partial cancellation of the oscillator's tail current variation [16]. In Fig. 17(d), the spur level is measured across the oscillator TR. The worst case spur level under the 50-mV_{pp} 5-MHz ripple is ≤ -59 dBc, while the calibrated value also follows the optimum one successfully on most occasions. The improvement after the calibration is higher than 30 dB across the TR.

The DPLL is measured with a 50-MHz external crystal reference clock and under the 50-mV_{pp} supply ripple. Fig. 18 shows the measured PN plot for both the integer- N and fractional- N channels around 4.8 GHz when $f_{\text{rip}} = f_{\text{ref}}/6$. The rms jitter integrated from 10 kHz to 30 MHz is 423 fs for the fractional- N operation and 409 fs for the integer- N operation.

The DPLL output spectrum is measured in three different scenarios. In Fig. 19(a), a 50-mV_{pp} 4.167 MHz (i.e., $f_{\text{ref}}/12$) ripple is applied to the oscillator and its calibration loop. The spur at f_{rip} due to the oscillator supply pushing is suppressed by 37 dB and reaches -62.7 dBc after the corresponding calibration is performed. The same ripple is then applied to the DPLL components except for the oscillator. As shown in Fig. 19(b), the spur at f_{rip} due to the delay variations of the loop components is -61.5 dBc, improving 31.6 dB due to the ripple pattern estimation and cancellation technique. Finally, the same ripple is applied to the entire DPLL. As shown in Fig. 19(c), when all calibration loops are enabled, the f_{rip} spur is reduced by 34.4 dB and reaches -60.5 dBc. In all three cases, the spur at f_{frac} due to the residue mismatch of the

resampling block is <-60 dBc after the mismatch calibration, while the spur at $2 \times f_{\text{frac}}$ originating from the nonlinearity of PD remains <-71.6 dBc. Extra spurs at $f_{\text{rip}} \pm f_{\text{frac}}$ and $2f_{\text{rip}} \pm f_{\text{frac}}$ with levels <-66 dBc could also be observed in Fig. 19(b) and (c). These spurs come from the undesired coupling between the supply of PD and the DCO output, both routed on the top metal layers with only ~ 10 μm spacing, and could also be observed when the oscillator is left free-running. In contrast, these spurs disappear when no ripple is applied to the PD supply. To suppress these spurs, the distance between the PD and the oscillator should be increased in future designs.

Similar measurements are performed when the frequency of the 50-mV_{pp} ripple is increased to $f_{\text{ref}}/3$ (i.e., 16.67 MHz). As can be gathered from Fig. 19(d)–(f), the f_{rip} spur is dominated by the oscillator supply pushing since the spur level due to the delay variations of the DPLL components is further suppressed by the low-pass transfer function of the loop. Fig. 20 shows the measured spur level at f_{frac} and $2f_{\text{frac}}$ across the fractional frequency, indicating that the mismatch calibration improves the in-band (out-of-band) f_{frac} spur level by about 9–14 dB (3–7 dB). Furthermore, considering both f_{frac} and $2f_{\text{frac}}$ spurs, a worst case spur level of -55 dBc is achieved after the calibration.

The oscillator and the DPLL are also measured under sawtooth ripples to better mimic the actual scenario of being directly powered by a switched-mode dc–dc converter. Fig. 21 shows the measured performance of the free-running DCO when a 50-mV_{pp} sawtooth ripple is applied to both the oscillator core and the calibration loop. Fig. 21(a) compares the oscillator spectrum before and after the calibration. At a 5-MHz ripple, the spur at the fundamental offset is reduced by 26.8 dB and reaches -57.3 dBc after the calibration. Fig. 21(b) plots the measured spur levels over the ripple frequency. In the entire span of 0.5–20 MHz, the highest spur is ≤ -46.8 dBc. The observed improvement after the automatic calibration is 13.3–24.6 dB for 4–17 MHz ripples. The entire oscillator TR was also scanned and the worst case spur level is ≤ -57.3 dBc under a 50-mV_{pp} 5 MHz sawtooth ripple; the calibrated value follows the optimum one in most cases. The improvement after the calibration is >26 dB across the TR.

Fig. 22 shows the measured PN and spurious performance for the fractional- N operation around 4.8 GHz under the 50-mV_{pp} sawtooth ripple when $f_{\text{rip}} = f_{\text{ref}}/6$. The integrated jitter is 428 fs for the fractional- N operation, while it is 411 fs for the integer- N operation. As expected, the PN performance of the DPLL under sawtooth ripples remains similar to that measured with sinusoidal ripples.

The measured output spectrum of the DPLL under a 50-mV_{pp} 4.167-MHz (i.e., $f_{\text{ref}}/12$) sawtooth ripple is shown in Fig. 23. Compared to the initial state where no calibration is performed, the spurs at f_{rip} and its harmonics induced by the ripple on the oscillator supply are suppressed after the supply pushing calibration, and the levels of these spurs are now mainly dominated by the variation of the output delay of loop components [see Fig. 23(a)]. When the ripple pattern estimation and cancellation algorithm is enabled, the spectrum in Fig. 23(a) shows that the spur at f_{rip} is suppressed significantly, while the spurs at its harmonics are also lowered.

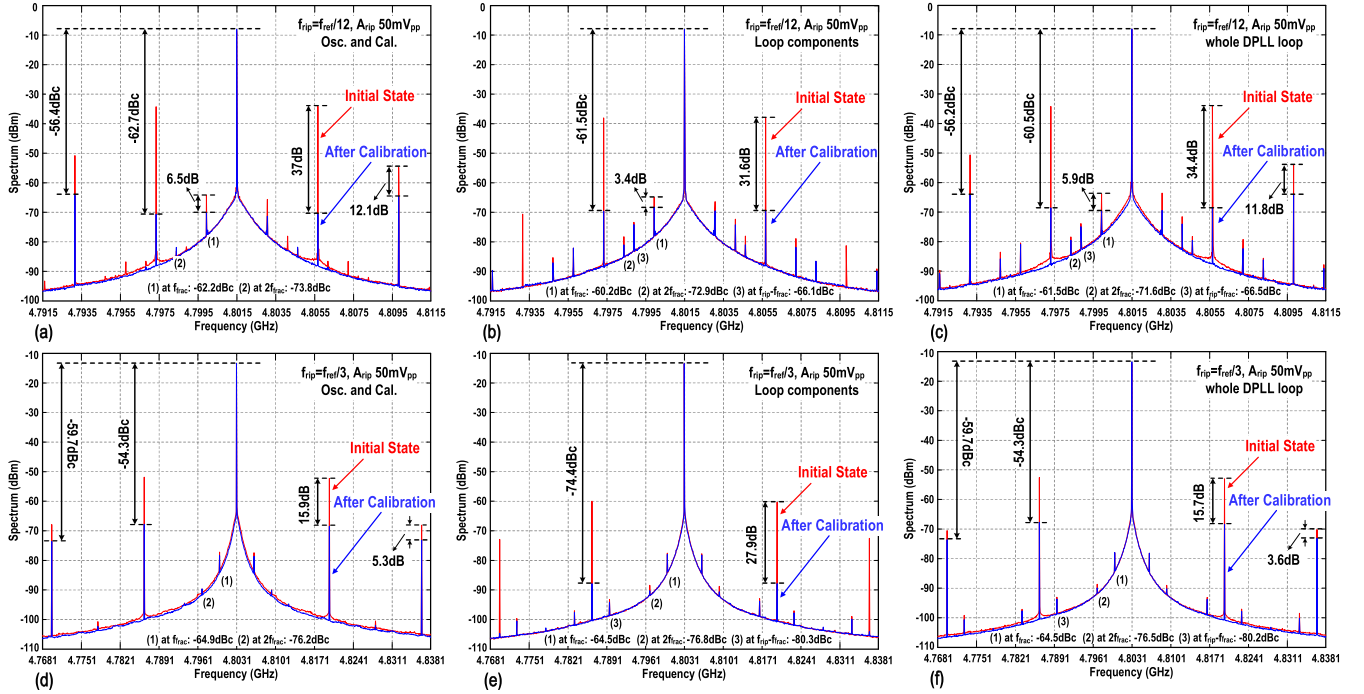


Fig. 19. Measured DPLL spectra when the 50-mV_{pp} $f_{ref}/12$ ($f_{ref}/3$) supply ripple is applied to (a) (d) oscillator and its calibration loop, (b) (e) loop components, and (c) (f) whole DPLL.

TABLE I
PERFORMANCE SUMMARY AND COMPARISON WITH PRIOR ART

	This Work	TCAS-II'12 [17]	TCAS-I'14 [2]	ESSCIRC'16 [11]	VLSI'17 [12]	ISSCC'16 [7]	JSSC'18 [38]	JSSC'21 [42]	TCAS-I'19 [41]	JSSC'21 [29]	
Tech. (nm)	40 (w/o UTM)	90	65	65	65	40	65	45 (PDSON)	130	130	
PLL Type	Digital Frac-N	Digital Int-N	Digital Int-N	Digital Int-N	Digital Int-N	Digital Int-N	Digital Frac-N	Analog Frac-N	Analog Frac-N	Analog Frac-N	
Osc. Type	LC	Ring	LC	LC	Ring	Ring	LC	LC	LC	LC	
Ripple applied to	whole loop	whole loop	GRO PD	Osc.	Osc.	Osc.	-	-	-	-	
Cancellation Tech.	SAR ADC based PD Ripple pattern cal. Feedforward K_{push} cal.	Cancel osc. supply noise through opposite sensitivities	GRO based supply noise monitor	FCW compensation	Noise suppression loop	Two constant-Gm biasing	-	-	-	-	
V_{DD} (V)	1.0	0.6	1.0	1.0	1.0	1.1	1.0/0.8	1.0	1.2	1.2	
f_{ref} (MHz)	50	50	26	30	50	200	26×2	100	50	50	
f_{out} (GHz)	4.47-5.14	0.8	1.4-1.8	3-5	3.2	3.2	2.0-2.8	7.7-9.1	1.9-2.3	1.8-2.3	
PN (dBc/Hz)	In-band (@100kHz)	-99.1	NA	-74 [#]	-103 [†]	-86.3	-105 [†]	-103.8	-120 ^{###}	-110.3	-109.2
	Out-band (@3MHz)	-117.5	NA	-98 [#]	-120 [†]	-108	-119 [†]	-128.0	-135 ^{###}	-127.9	-132 [†]
PN _{norm} (dBc/Hz)	In-band (@100kHz)	-99.1	NA	-58.8 [#]	-100.4 [†]	-82.8	-101.5 [†]	-97.9	-118.3 ^{###}	-103.6	-102.0
	Out-band (@3MHz)	-117.5	NA	-82.8 [#]	-117.4 [†]	-104.5	-115.5 [†]	-122.2	-133.3 ^{###}	-121.2	-124.9 [†]
Integrated Jitter (ps)	0.428	34.1 [†]	NA	0.52	7.8	3.85	0.53	0.135	0.291	0.414	
Frac. Spur (dBc)	<-55	-	-	-	-	-	<-56	<-55 ^{###}	<-48.6	-57	
Frac. Spur _{norm} (dBc)	<-55	-	-	-	-	-	<-50.1	<-47.9	<-41.9	-49.9	
Ripple Amplitude	50mV _{pp}	50mV _{pp}	200mV _{pp}	NA	20mV _{pp}	50mV _{pp}	-	-	-	-	
f_{rip} (MHz)	$f_{ref}/12$ $f_{ref}/6$ $f_{ref}/3$	1-100	1.0	0.5-10	0.5 2.5 20	0.1	-	-	-	-	
Spur @ f_{rip} (dBc)	sinewave saw-tooth	-60.5 -61.6 -54.3	NA	-49 [#]	NA	-63 -45.5 -59.2	-28 [†]	-	-	-	
Power (mW)	3.25	0.66	11.3	21.3	2.73	2.915	0.98	4.5	3.2	2.8	
FoM _{int} (dB)	-242.3	-211.1	NA	-234.6	-217.8	-217.6	-245.4	-247.8	-245.7	-243.2	
Area (mm ²)	0.39	0.0221	0.65	0.63	0.047	0.0216	0.23	0.1 [†]	0.45	0.4	

[#]Phase noise normalized to 4.8GHz, PN_{norm}=PN+20×log₁₀(4.8GHz/ f_{out}) [†]Spur level normalized to 4.8GHz, Spur_{norm}=Spur+20×log₁₀(4.8GHz/ f_{out}) ^{###}FoM_{int}=10×log₁₀((σ_{rms})²×Power/1mW/($f_{ref}/50$ MHz)) [56]

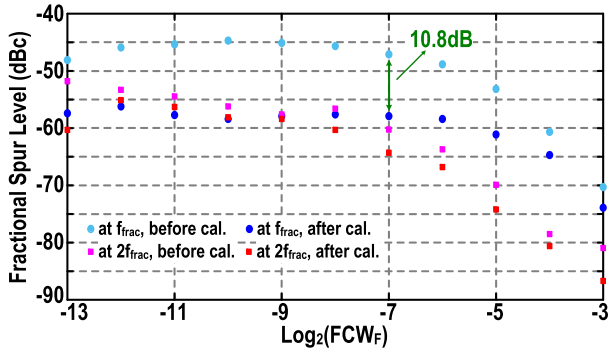
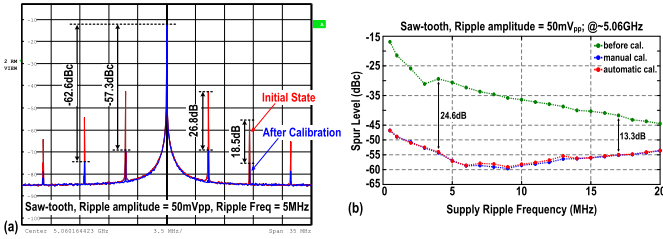
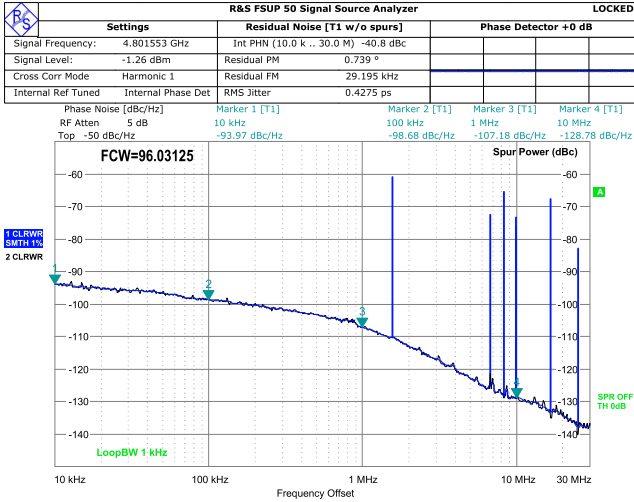
^{*}Measured at 280MHz output (f_{ref} =17.5MHz) ^{##}Measured after divide by 2 at 832MHz ^{††}Estimated from measurement result [‡]Excluding the integrated loop filter

^{###}Estimated from measurement after divide by 2 at ~3.95GHz ^{####}Measured after divide by 4 at ~2.12558GHz

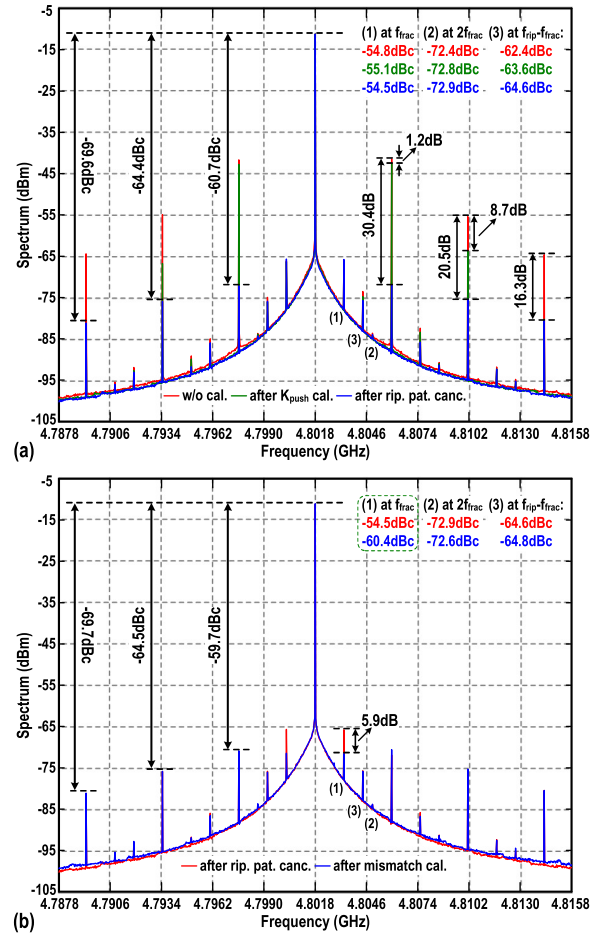
In contrast, the spur level at f_{frac} remains unaffected during these calibrations. To suppress this spur, the mismatch calibration is then enabled, and the spur level at f_{frac} is reduced from -54.5 to -60.4 dBc, as shown in Fig. 23(b). During the mismatch calibration, the levels of spurs at f_{rip} and its harmonics unchanged. The spur level at $2f_{frac}$ due to

the PD nonlinearity also remains at ~ -72.6 dBc during these calibrations.

Table I summarizes the performance of the proposed DPLL and compares it with state-of-the-art designs. We first compare the performance of the prototype under supply ripple to state-of-the-art low-power (<5 mW) fractional-N PLLs


 Fig. 20. Measured fractional spur levels versus fractional FCW (FCW_F).

 Fig. 21. Measurements of the free-running DCO under sawtooth ripples: (a) spectrum before and after the automatic calibration in face of a 50-mV_{pp} 5-MHz ripple; (b) worst case spur levels across the ripple frequency for both the manual and automatic calibrations.

 Fig. 22. Measured DPLL PN at the fractional- N channel around 4.8 GHz under sawtooth ripples.

under a clean supply [29], [38], [41], [42]. The normalized FoM (FoM_R , defined at the bottom of Table I) is ~ 3 dB worse compared to [38] and [41], while it is ~ 5 dB worse compared to [42] implemented in the silicon on insulator (SOI) technology. This is partly due to the fact that no ultra-thick top metal layer is available in the technology used, limiting the Q -factor of the DCO. Moreover, in order not to offset the advantages of removing the LDOs, no external capacitor is used to filter out the noise of the biasing current in the slope generator and current DAC; this, however, increases the contribution of PD's circuit noise to the in-band PN by about 40% as per simulations. In contrast, for example, the


 Fig. 23. Measured DPLL spectrum under a 50-mV_{pp} $f_{ref}/12$ sawtooth ripple at the initial state [red curve in (a)] and after enabling the oscillator supply pushing calibration [green curve in (a)], after enabling the ripple pattern estimation and cancellation [blue curve in (a) / red curve in (b)], and after enabling the divider resampler mismatch calibration [blue curve in (b)] sequentially.

design in [42] uses several external tunable reference voltages to charge/discharge the capacitors in its sampling PD and the following CDAC, which is difficult to integrate on-chip. Next, our prototype is compared to designs with “dirty” supplies [2], [7], [11], [12], [17]. The f_{rip} spur of the prototype is the lowest under a large 50-mV_{pp} supply ripple. Meanwhile, to the best of our knowledge, the proposed design is the first fractional- N PLL that can successfully operate under the supply ripples with acceptable performance.

VI. CONCLUSION

This article demonstrates a fractional- N DPLL that is insensitive to supply ripples, thereby enabling a direct connection to a dc-dc converter. To tolerate the supply ripple, the feed-forward ripple replication and cancellation technique with an improved calibration loop is adopted to reduce the supply pushing of the LC oscillator. The output of the MMDIV, which is driven by a second-order $\Delta\Sigma$ modulator, is resampled by both edges of the oscillator output to halve the input range of the following slope generator. This facilitates a linear and supply-insensitive conversion from time to voltage domain by the slope generator. Meanwhile, a current DAC compensates

for the excursion due to the fractional- N operation in order to limit the dynamic range of the SAR ADC that quantizes the phase error. A ripple pattern estimation and cancellation algorithm is integrated to cancel the phase error induced by the delay variations of the loop component under the supply ripple from the ADC output so that it would not modulate the oscillator. Prototyped in 40-nm CMOS, the DPLL exhibits 428-fs rms jitter and <-55 -dBc fractional spur, while the ripple spur is also <-54 dBc.

APPENDIX A

Since the supply perturbation is relatively small, it is reasonable to assume that the delay variation, Δt_{VDD} , is proportional to the ripple amplitude A_{rip} , i.e.,

$$\Delta t_{\text{VDD}} = K_{\text{VDD}} A_{\text{rip}}. \quad (12)$$

Hence, the peak-to-peak phase deviation presented at the PD input is

$$\Delta \phi_{\text{VDD}} = 2\pi \cdot \frac{K_{\text{VDD}} A_{\text{rip}}}{T_{\text{CKV}}} \quad (13)$$

inducing an extra phase variation at the PLL output with a peak-to-peak amplitude of

$$\Delta \phi_{\text{VDD,out}} = 2\pi \cdot \frac{K_{\text{VDD}} A_{\text{rip}}}{T_{\text{CKV}}} \cdot 10^{\text{TF}_{\text{loop}}/20}. \quad (14)$$

Note that ϕ_{VDD} is normalized to f_{osc} directly, and thus, $\text{TF}_{\text{loop}} \approx 1$ at low frequency offsets, as shown in Fig. 1(b). Instead, if ϕ_{VDD} is normalized to f_{ref} , TF_{loop} should be multiplied by the division ratio, resulting in the same expression shown in (14). Based on (14), the output signal of the PLL, x_{PLL} , is expressed as

$$x_{\text{PLL}} = A_{\text{osc}} \sin\left(\omega_{\text{osc}} t + \frac{\Delta \phi_{\text{VDD,out}}}{2} \sin(\omega_{\text{rip}} t)\right) \quad (15)$$

where A_{osc} is the amplitude of CKV. Given that $|\phi_{\text{VDD,out}}|$ is typically much less than $\pi/6$, (15) could then be approximated as

$$x_{\text{PLL}} \approx A_{\text{osc}} \sin(\omega_{\text{osc}} t) + A_{\text{osc}} \cdot \frac{\Delta \phi_{\text{VDD,out}}}{4} \cdot (\sin[(\omega_{\text{osc}} + \omega_{\text{rip}})t] - \sin[(\omega_{\text{osc}} - \omega_{\text{rip}})t]). \quad (16)$$

Combining (16) and (14), the spur level induced by the delay variation of MMDIV under supply ripple is calculated as

$$\begin{aligned} S_{\text{dly}} &= 20 \cdot \log_{10}\left(\frac{\phi_{\text{VDD,out}}}{4}\right) \\ &= 20 \cdot \log_{10}\left(\frac{\pi \cdot K_{\text{VDD}} \cdot A_{\text{rip}}}{2T_{\text{CKV}}}\right) + \text{TF}_{\text{loop}} \end{aligned} \quad (17)$$

which is the very result presented in (2).

APPENDIX B

As shown in (5), the output delay of DTC is modulated by the supply ripple as

$$\Delta t_{\text{DTC}} = T_{\text{CKV}} \cdot \text{sawtooth}\{\omega_{\text{frac}} t\} (1 + 0.5\beta A_{\text{rip}} \sin(\omega_{\text{rip}} t)) \quad (18)$$

in which sawtooth $\{\omega_{\text{frac}} t\}$ represents the sawtooth waveform with a fundamental frequency of f_{frac} and a peak-to-peak magnitude of 1. Its Fourier series is

$$\text{sawtooth}\{\omega_{\text{frac}} t\} = \frac{1}{2} + \sum_{n=1}^{\infty} \frac{1}{n\pi} \cdot \sin(n\omega_{\text{frac}} t). \quad (19)$$

The first term in (19) corresponds to a delay offset, which cancels with the dc value of the delay between REF and DIV in the locking state and can be ignored in the following analysis. The second term of (19) will generate intermodulation terms, and we will focus on its fundamental component ($n = 1$) since it has the largest magnitude. By replacing this fundamental component into (18), we have

$$\begin{aligned} \Delta t_{\text{DTC}} &= T_{\text{CKV}} \cdot \frac{1}{\pi} \sin(\omega_{\text{frac}} t) \cdot (1 + 0.5\beta A_{\text{rip}} \sin(\omega_{\text{rip}} t)) \\ &= \frac{T_{\text{CKV}}}{\pi} \sin(\omega_{\text{frac}} t) + \frac{\beta A_{\text{rip}} T_{\text{CKV}}}{4\pi} \\ &\quad \cdot (\cos[(\omega_{\text{rip}} - \omega_{\text{frac}})t] - \cos[(\omega_{\text{rip}} + \omega_{\text{frac}})t]) \end{aligned} \quad (20)$$

which is exactly the result shown in (6). The first term in (20) compensates for the deterministic delay variation between REF and DIV due to the fractional- N operation, while its second terms contains intermodulation, potentially generating in-band spurs at the PLL output. From (20), the phase fluctuation corresponding to the intermodulation terms is

$$\Delta \phi_{\text{DTC,int}} = \frac{\beta A_{\text{rip}}}{2} \cdot (\cos[(\omega_{\text{rip}} - \omega_{\text{frac}})t] - \cos[(\omega_{\text{rip}} + \omega_{\text{frac}})t]). \quad (21)$$

Hence, the output signal of the PLL could be expressed as

$$\begin{aligned} x_{\text{PLL}} &= A_{\text{osc}} \sin(\omega_{\text{osc}} t + \Delta \phi_{\text{DTC,int}}) \\ &= A_{\text{osc}} \sin\left(\omega_{\text{osc}} t + \frac{\beta A_{\text{rip}}}{2} \cdot (\cos[(\omega_{\text{rip}} - \omega_{\text{frac}})t] - \cos[(\omega_{\text{rip}} + \omega_{\text{frac}})t])\right). \end{aligned} \quad (22)$$

Since $\beta A_{\text{rip}}/2$ is much less than $\pi/6$, (22) could then be approximated as

$$\begin{aligned} x_{\text{PLL}} &\approx A_{\text{osc}} \sin(\omega_{\text{osc}} t) \\ &\quad + A_{\text{osc}} \cdot \frac{\beta A_{\text{rip}}}{4} \cdot (\cos[(\omega_{\text{osc}} + \omega_{\text{int,-}})t] + \cos[(\omega_{\text{osc}} - \omega_{\text{int,-}})t]) \\ &\quad - A_{\text{osc}} \cdot \frac{\beta A_{\text{rip}}}{4} \cdot (\cos[(\omega_{\text{osc}} + \omega_{\text{int,+}})t] + \cos[(\omega_{\text{osc}} - \omega_{\text{int,+}})t]) \end{aligned} \quad (23)$$

in which $\omega_{\text{int,-}} = \omega_{\text{rip}} - \omega_{\text{frac}}$ and $\omega_{\text{int,+}} = \omega_{\text{rip}} + \omega_{\text{frac}}$. From (23), it can be concluded that the intermodulation terms in (20) would generate spurs at $f_{\text{rip}} \pm f_{\text{frac}}$ at the PLL output, and when they fall in-band, the spur level should be $20\log_{10}(\beta \cdot A_{\text{rip}}/4)$.

ACKNOWLEDGMENT

The authors would like to thank Zhong Gao from the Delft University of Technology and Yao-Hong Liu and Johan Dijkhuis from the imec-nl Holst Center for technical discussion and assistance. They would also like to thank Atef Akhnouk and Zu Yao Chang for their help with the tape-out and chip bonding.

REFERENCES

- [1] J. Prummel *et al.*, "A 10 mW Bluetooth low-energy transceiver with on-chip matching," *IEEE J. Solid-State Circ.*, vol. 50, no. 12, pp. 3077–3088, Dec. 2015.
- [2] Y. Liu, Y. Han, W. Rhee, T.-Y. Oh, and Z. Wang, "A PSRR enhancing method for GRO TDC based clock generation systems," *IEEE Trans. Circuits Syst. I, Reg. Papers*, vol. 61, no. 3, pp. 680–688, Mar. 2014.
- [3] A. Urso, Y. Chen, J. F. Dijkhuis, Y.-H. Liu, M. Babaie, and W. A. Serdijn, "Analysis and design of power supply circuits for RF oscillators," *IEEE Trans. Circuits Syst. I, Reg. Papers*, vol. 67, no. 12, pp. 4233–4246, Dec. 2020.
- [4] X. Gao, E. A. M. Klumperink, P. F. J. Geraedts, and B. Nauta, "Jitter analysis and a benchmarking figure-of-merit for phase-locked loops," *IEEE Trans. Circuits Syst. II, Exp. Briefs*, vol. 56, no. 2, pp. 117–121, Feb. 2009.
- [5] Y. C. Huang, C. F. Liang, H. S. Huang, and P. Y. Wang, "A 2.4 GHz ADPLL with digital-regulated supply-noise-insensitive and temperature-self-compensated ring DCO," in *IEEE Int. Solid-State Circuits Conf. (ISSCC) Dig. Tech. Papers*, Feb. 2014, pp. 270–271.
- [6] J. Liu *et al.*, "A 0.012 mm² 3.1 mW bang-bang digital fractional-N PLL with a power-supply-noise cancellation technique and a walking-one-phase-selection fractional frequency divider," in *IEEE Int. Solid-State Circuits Conf. (ISSCC) Dig. Tech. Papers*, Feb. 2014, pp. 268–269.
- [7] C. W. Yeh, C. E. Hsieh, and S. I. Liu, "A 3.2 GHz digital phase-locked loop with background supply-noise cancellation," in *IEEE Int. Solid-State Circuits Conf. (ISSCC) Dig. Tech. Papers*, Jan. 2016, pp. 332–333.
- [8] K. Y. J. Shen *et al.*, "A 0.17-to-3.5 mW 0.15-to-5 GHz SoC PLL with 15 dB built-in supply noise rejection and self-bandwidth control in 14 nm CMOS," in *IEEE Int. Solid-State Circuits Conf. (ISSCC) Dig. Tech. Papers*, Jan. 2016, pp. 330–331.
- [9] T. Wu, K. Mayaram, and U.-K. Moon, "An on-chip calibration technique for reducing supply voltage sensitivity in ring oscillators," *IEEE J. Solid-State Circuits*, vol. 42, no. 4, pp. 775–783, Apr. 2007.
- [10] C.-W. Tien and S.-I. Liu, "A digital phase-locked loop with background supply voltage sensitivity minimization," *IEEE Trans. Circuits Syst. I, Reg. Papers*, vol. 65, no. 6, pp. 1830–1839, Jun. 2018.
- [11] C.-R. Ho and M. S.-W. Chen, "Interference-induced DCO spur mitigation for digital phase locked loop in 65-nm CMOS," in *Proc. 42nd Eur. Solid-State Circuits Conf. (ESSCIRC)*, Sep. 2016, pp. 213–216.
- [12] D. Kim and S. Cho, "A supply noise insensitive PLL with a rail-to-rail swing ring oscillator and a wideband noise suppression loop," in *Proc. Symp. VLSI Circuits*, Jun. 2017, pp. C180–C181.
- [13] S. S. Nagam and P. R. Kinget, "A low-jitter ring-oscillator phase-locked loop using feedforward noise cancellation with a sub-sampling phase detector," *IEEE J. Solid-State Circuits*, vol. 53, no. 3, pp. 703–714, Mar. 2018.
- [14] A. Elshazly, R. Inti, W. Yin, B. Young, and P. K. Hanumolu, "A 0.4-to-3 GHz digital PLL with PVT insensitive supply noise cancellation using deterministic background calibration," *IEEE J. Solid-State Circuits*, vol. 46, no. 12, pp. 2759–2771, Dec. 2011.
- [15] X. Gui, B. Tang, R. Tang, D. Li, and L. Geng, "Low-supply sensitivity LC VCOs with complementary varactors," *IEEE Trans. Very Large Scale Integr. (VLSI) Syst.*, vol. 28, no. 7, pp. 1589–1599, Jul. 2020.
- [16] Y. Chen *et al.*, "A supply pushing reduction technique for LC oscillators based on ripple replication and cancellation," *IEEE J. Solid-State Circuits*, vol. 54, no. 1, pp. 240–252, Jan. 2019.
- [17] K.-H. Cheng, J.-C. Liu, and H.-Y. Huang, "A 0.6-V 800-MHz all-digital phase-locked loop with a digital supply regulator," *IEEE Trans. Circuits Syst. II, Exp. Briefs*, vol. 59, no. 12, pp. 888–892, Dec. 2012.
- [18] W. Rhee, K. A. Jenkins, J. Liobe, and H. Ainspan, "Experimental analysis of substrate noise effect on PLL performance," *IEEE Trans. Circuits Syst. II, Exp. Briefs*, vol. 55, no. 7, pp. 638–642, Jul. 2008.
- [19] P. V. Brennan, P. M. Radmore, and D. Jiang, "Intermodulation-borne fractional-N frequency synthesizer spurious components," *IEE Proc. Circuits, Devices Syst.*, vol. 151, no. 6, pp. 536–542, Dec. 2004.
- [20] D. Murphy, H. Darabi, and H. Wu, "Implicit common-mode resonance in LC oscillators," *IEEE J. Solid-State Circuits*, vol. 52, no. 3, pp. 812–821, Mar. 2017.
- [21] D. Liao *et al.*, "An 802.11a/b/g/n digital fractional- N PLL with automatic TDC linearity calibration for spur cancellation," *IEEE J. Solid-State Circuits*, vol. 52, no. 5, pp. 1210–1220, May 2017.
- [22] A. Elkholy, T. Anand, W.-S. Choi, A. Elshazly, and P. K. Hanumolu, "A 3.7 mW low-noise wide-bandwidth 4.5 GHz digital fractional-N PLL using time amplifier-based TDC," *IEEE J. Solid-State Circuits*, vol. 50, no. 4, pp. 867–881, Apr. 2015.
- [23] H. Park, C. Hwang, T. Seong, Y. Lee, and J. Choi, "A 365 fs_{rms}-jitter and -63 dBc-fractional spur 5.3 GHz-ring-DCO-based fractional-N DPLL using a DTC second/third-order nonlinearity cancelation and a probability-density-shaping $\Delta\Sigma$," in *IEEE Int. Solid-State Circuits Conf. (ISSCC) Dig. Tech. Papers*, Feb. 2021, pp. 442–444.
- [24] W. Chang and T. Lee, "A 5 GHz fractional- N ADC-based digital phase-locked loops with -243.8 dB FOM," *IEEE Trans. Circuits Syst. I, Reg. Papers*, vol. 63, no. 11, pp. 1845–1853, Nov. 2016.
- [25] A. Arakali, S. Gondi, and P. K. Hanumolu, "Analysis and design techniques for supply-noise mitigation in phase-locked loops," *IEEE Trans. Circuits Syst. I, Reg. Papers*, vol. 57, no. 11, pp. 2880–2889, Nov. 2010.
- [26] D. Turker *et al.*, "A 7.4-to-14 GHz PLL with 54 fs_{rms} jitter in 16 nm FinFET for integrated RF-data-converter SoCs," in *IEEE Int. Solid-State Circuits Conf. (ISSCC) Dig. Tech. Papers*, Feb. 2018, pp. 378–380.
- [27] D.-G. Lee and P. P. Mercier, "A sub-mW 2.4-GHz active-mixer-adopted sub-sampling PLL achieving an FoM of -256 dB," *IEEE J. Solid-State Circuits*, vol. 55, no. 6, pp. 1542–1552, Jun. 2020.
- [28] Y.-L. Hsueh *et al.*, "A 0.29 mm² frequency synthesizer in 40 nm CMOS with 0.19 ps_{rms} jitter and <-100 dBc reference spur for 802.11ac," in *IEEE Int. Solid-State Circuits Conf. (ISSCC) Dig. Tech. Papers*, Feb. 2014, pp. 472–473.
- [29] H. Su, J. Tao, S. D. Balon, and C.-H. Heng, "A 2.3 GHz 2.8 mW sampling $\Delta\Sigma$ PLL achieving -110 dBc/Hz in-band phase noise and 500 MHz FMCW chirp," *IEEE J. Solid-State Circuits*, vol. 56, no. 11, pp. 3458–3469, Jul. 2021.
- [30] S. Levantino, G. Marzin, C. Samori, and A. L. Lacaita, "A wideband fractional-N PLL with suppressed charge-pump noise and automatic loop filter calibration," *IEEE J. Solid-State Circuits*, vol. 48, no. 10, pp. 2419–2429, Oct. 2013.
- [31] M. Ferriss, B. Sadhu, A. Rylakov, H. Ainspan, and D. Friedman, "A 12-to-26 GHz fractional-N PLL with dual continuous tuning LC-D/VCOs," in *IEEE Int. Solid-State Circuits Conf. (ISSCC) Dig. Tech. Papers*, Jan. 2016, pp. 196–198.
- [32] Z. Chen *et al.*, "Sub-sampling all-digital fractional-N frequency synthesizer with -111 dBc/Hz in-band phase noise and an FOM of -242 dB," in *IEEE Int. Solid-State Circuits Conf. (ISSCC) Dig. Tech. Papers*, Feb. 2015, pp. 268–269.
- [33] X. Gao *et al.*, "A 2.7-to-4.3 GHz, 0.16 ps_{rms}-jitter, -246.8 dB-FOM, digital fractional-N sampling PLL in 28 nm CMOS," in *IEEE Int. Solid-State Circuits Conf. (ISSCC) Dig. Tech. Papers*, Jan. 2016, pp. 174–175.
- [34] Z. Xu *et al.*, "A 3.6 GHz low-noise fractional-N digital PLL using SAR-ADC-based TDC," *IEEE J. Solid-State Circuits*, vol. 51, no. 10, pp. 2345–2356, Oct. 2016.
- [35] Y. Hu *et al.*, "A 21.7-to-26.5 GHz charge-sharing locking quadrature PLL with implicit digital frequency-tracking loop achieving 75 fs jitter and -250 dB FoM," in *IEEE Int. Solid-State Circuits Conf. (ISSCC) Dig. Tech. Papers*, Feb. 2020, pp. 276–278.
- [36] J. Kim *et al.*, "A 104 fs_{rms}-jitter and -61 dBc-fractional spur 15 GHz fractional-N subsampling PLL using a voltage-domain quantization-error cancelation technique," in *IEEE Int. Solid-State Circuits Conf. (ISSCC) Dig. Tech. Papers*, vol. 64, Feb. 2021, pp. 448–450.
- [37] J. Z. Ru, C. Palattella, P. Geraedts, E. Klumperink, and B. Nauta, "A high-linearity digital-to-time converter technique: Constant-slope charging," *IEEE J. Solid-State Circuits*, vol. 50, no. 6, pp. 1412–1423, Jun. 2015.
- [38] H. Liu, D. Tang, Z. Sun, W. Deng, H. C. Ngo, and K. Okada, "A sub-mW fractional-N ADPLL with FOM of -246 dB for IoT applications," *IEEE J. Solid-State Circuits*, vol. 53, no. 12, pp. 3540–3552, Dec. 2018.
- [39] P. Chen, F. Zhang, Z. Zong, S. Hu, T. Siriburanon, and R. B. Staszewski, "A 31- μ W, 148-fs step, 9-bit capacitor-DAC-based constant-slope digital-to-time converter in 28-nm CMOS," *IEEE J. Solid-State Circuits*, vol. 54, no. 11, pp. 3075–3085, Nov. 2019.
- [40] L. Wu, T. Burger, P. Schonle, and Q. Huang, "A power-efficient fractional-N DPLL with phase error quantized in fully differential-voltage domain," *IEEE J. Solid-State Circuits*, vol. 56, no. 4, pp. 1254–1264, Apr. 2021.

- [41] J. Tao and C. Heng, "A 2.2-GHz 3.2-mW DTC-free sampling $\Delta\Sigma$ fractional-N PLL with -110 -dBc/Hz in-band phase noise and -246 -dB FoM and -83 -dBc reference spur," *IEEE Trans. Circuits Syst. I, Reg. Papers*, vol. 66, no. 9, pp. 3317–3329, Sep. 2019.
- [42] D. Liao and F. F. Dai, "A fractional-N reference sampling PLL with linear sampler and CDAC based fractional spur cancellation," *IEEE J. Solid-State Circuits*, vol. 56, no. 3, pp. 694–704, Mar. 2021.
- [43] I. Galton, "Why dynamic-element-matching DACs work," *IEEE Trans. Circuits Syst. II, Exp. Briefs*, vol. 57, no. 2, pp. 69–74, Feb. 2010.
- [44] A. M. Abo and P. R. Gary, "A 1.5-V, 10-bit, 14.3-MS/s CMOS pipeline analog-to-digital converter," *IEEE J. Solid-State Circuits*, vol. 34, no. 5, pp. 599–606, May 1999.
- [45] C.-C. Liu, S.-J. Chang, G.-Y. Huang, and Y.-Z. Lin, "A 10-bit 50-MS/s SAR ADC with a monotonic capacitor switching procedure," *IEEE J. Solid-State Circuits*, vol. 45, no. 4, pp. 731–740, Apr. 2010.
- [46] C. S. Vaucher, I. Ferencic, M. Locher, S. Sedvallson, U. Voegeli, and Z. Wang, "A family of low-power truly modular programmable dividers in standard $0.35\text{-}\mu\text{m}$ CMOS technology," *IEEE J. Solid-State Circuits*, vol. 35, no. 7, pp. 1039–1045, Jul. 2000.
- [47] D. Tasca, M. Zanuso, G. Marzin, S. Levantino, C. Samori, and A. L. Lacaita, "A 2.9–4.0-GHz fractional-N digital PLL with bang-bang phase detector and $560\text{-fs}_{\text{rms}}$ integrated jitter at 4.5-mW power," *IEEE J. Solid-State Circuits*, vol. 46, no. 12, pp. 2745–2758, Dec. 2011.
- [48] D. Tasca, M. Zanuso, S. Levantino, C. Samori, and A. L. Lacaita, "Low-power divider retiming in a 3–4 GHz fractional-N PLL," *IEEE Trans. Circuits Syst. II, Exp. Briefs*, vol. 58, no. 4, pp. 200–204, Apr. 2011.
- [49] W. Wu *et al.*, "A 14 nm analog sampling fractional-N PLL with a digital-to-time converter range-reduction technique achieving 80 fs integrated jitter and 93 fs at near-integer channels," in *IEEE Int. Solid-State Circuits Conf. (ISSCC) Dig. Tech. Papers*, Feb. 2021, pp. 444–446.
- [50] C. Samori, M. Zanuso, S. Levantino, and A. L. Lacaita, "Multipath adaptive cancellation of divider non-linearity in fractional-N PLLs," in *Proc. IEEE Int. Symp. Circuits Syst. (ISCAS)*, May 2011, pp. 418–421.
- [51] C.-R. Ho and M. S.-W. Chen, "A digital PLL with feedforward multi-tone spur cancellation scheme achieving <-73 dBc fractional spur and <-110 dBc reference spur in 65 nm CMOS," *IEEE J. Solid-State Circuits*, vol. 51, no. 12, pp. 3216–3230, Dec. 2016.
- [52] A. Urso *et al.*, "A switched-capacitor DC-DC converter powering an LC oscillator to achieve 85% system peak power efficiency and -65 dBc spurious tones," *IEEE Trans. Circuits Syst. I, Reg. Papers*, vol. 67, no. 11, pp. 3764–3777, Nov. 2020.
- [53] C. J. Park, M. Onabajo, and J. Silva-Martinez, "External capacitor-less low drop-out regulator with 25 dB superior power supply rejection in the 0.4–4 MHz range," *IEEE J. Solid-State Circuits*, vol. 49, no. 2, pp. 486–501, Feb. 2014.
- [54] S. Bu, K. N. Leung, Y. Lu, J. Guo, and Y. Zheng, "A fully integrated low-dropout regulator with differentiator-based active zero compensation," *IEEE Trans. Circuits Syst. I, Reg. Papers*, vol. 65, no. 10, pp. 3578–3591, Oct. 2018.
- [55] J. Jiang, W. Shu, and J. S. Chang, "A 65-nm CMOS low dropout regulator featuring >60 -dB PSRR over 10-MHz frequency range and 100-mA load current range," *IEEE J. Solid-State Circuits*, vol. 53, no. 8, pp. 2331–2342, Aug. 2018.
- [56] J. Zhu, R. K. Nandwana, G. Shu, A. Elkholy, S. J. Kim, and P. K. Hanumolu, "A 0.0021 mm^2 1.82 mW 2.2 GHz PLL using time-based integral control in 65 nm CMOS," *IEEE J. Solid-State Circuits*, vol. 52, no. 1, pp. 8–20, Jan. 2017.



Yue Chen (Student Member, IEEE) received the B.Eng. degree in microelectronics and the M.Eng. degree in electronic science and technology from Xi'an Jiaotong University, Xi'an, China, in 2011 and 2014, respectively. He is currently pursuing the Ph.D. degree in electronic engineering with the Department of Microelectronics, Delft University of Technology, Delft, The Netherlands.

His current research interests include frequency synthesizer techniques and integrated circuits for wireless communications.



Jiang Gong (Student Member, IEEE) received the B.Sc. degree in electrical engineering from Jilin University, Changchun, China, in 2015, and the M.Sc. degree (*cum laude*) in microelectronics from the Delft University of Technology, Delft, The Netherlands, in 2017, where he is currently pursuing the Ph.D. degree.

His research focuses on high-spectral-purity and wide-tuning-range cryogenic frequency synthesizers for quantum computing applications.



Robert Bogdan Staszewski (Fellow, IEEE) was born in Białystok, Poland. He received the B.Sc. (*summa cum laude*), M.Sc., and Ph.D. degrees in electrical engineering from The University of Texas at Dallas, Richardson, TX, USA, in 1991, 1992, and 2002, respectively.

From 1991 to 1995, he was with Alcatel Network Systems, Richardson, involved in SONET cross-connected systems for fiber-optics communications. He joined Texas Instruments Inc., Dallas, TX, USA, in 1995, where he was an elected Distinguished Member of Technical Staff (limited to 2% of technical staff). From 1995 to 1999, he was engaged in advanced CMOS read channel development for hard disk drives. In 1999, he co-started the Digital RF Processor (DRP) Group, Texas Instruments, with a mission to invent new digitally intensive approaches to traditional RF functions for integrated radios in deeply scaled CMOS technology. He was appointed as the CTO of the DRP Group from 2007 to 2009. In 2009, he joined the Delft University of Technology, Delft, The Netherlands, where he currently holds a guest appointment of Full Professor (*Antoni van Leeuwenhoek Hoogleraar*). Since 2014, he has been a Full Professor with University College Dublin (UCD), Dublin, Ireland. He is a Co-Founder of a startup company, Equal Labs, with design centers located in Silicon Valley and Dublin, Ireland, aiming to produce single-chip CMOS quantum computers. He has authored or coauthored five books, eight book chapters, and 150 journals and 210 conference publications. He holds 210 issued U.S. patents. His research interests include nanoscale CMOS architectures and circuits for frequency synthesizers, transmitters and receivers, as well as quantum computers.

Dr. Staszewski was a recipient of the 2012 IEEE Circuits and Systems Industrial Pioneer Award. He serves on the Technical Program Committee of the VLSI Symposium on Circuits.



Masoud Babaie (Member, IEEE) received the B.Sc. degree (Hons.) from the Amirkabir University of Technology, Tehran, Iran, in 2004, the M.Sc. degree from the Sharif University of Technology, Tehran, in 2006, and the Ph.D. degree (*cum laude*) from the Delft University of Technology, Delft, The Netherlands, in 2016, all in electrical engineering.

From 2006 to 2011, he was with the Kavoshcom Research and Development Group, Tehran, where he was involved in designing wireless communication systems. From 2014 to 2015, he was a Visiting Scholar Researcher at the Berkeley Wireless Research Center, Berkeley, CA, USA. In 2016, he joined the Delft University of Technology, where he is currently a tenured Assistant Professor. He has authored or coauthored one book, three book chapters, 11 patents, and over 70 technical articles. His research interests include RF/millimeter-wave integrated circuits and systems for wireless communications and cryogenic electronics for quantum computation.

Dr. Babaie serves on the Technical Program Committee of the IEEE International Solid-State Circuits Conference (ISSCC) and the Co-Chair for the Emerging Computing Devices and Circuits Subcommittee of the IEEE European Solid-State Circuits Conference (ESSCIRC). He was a co-recipient of the 2015–2016 IEEE Solid-State Circuits Society Pre-Doctoral Achievement Award, the 2019 IEEE ISSCC Best Demo Award, and the 2020 IEEE ISSCC Jan Van Vessel Award for Outstanding European Paper. He received the Veni Award from the Netherlands Organization for Scientific Research (NWO) in 2019.